Geometric and Electrochemical Characteristics of LiNi$_{1/3}$Mn$_{1/3}$Co$_{1/3}$O$_2$ Electrode with Different Calendering Conditions

Huixiao Kang[a], Cheolwoong Lim[a], Tianyi Li[a], Yongzhu Fu[a], Bo Yan[b], Nicole Houston[c], Vincent De Andrade[d], Francesco De Carlo[d], Likun Zhu[a*]
##Email##likzhu@iupui.edu##/Email##

[a]Department of Mechanical Engineering, Indiana University–Purdue University Indianapolis, Indianapolis, Indiana 46202, USA
[b]School of Materials Science and Engineering, Shanghai Jiao Tong University, Shanghai, 200030, China
[c]Harris Academy, Brownsburg School District, Indianapolis, Indiana 46214, USA
[d]Advanced Photon Source, Argonne National Laboratory, Argonne, Illinois 60439, USA

[*]Corresponding Author: Department of Mechanical Engineering Indiana University Purdue University Indianapolis 723 W. Michigan Street, Room SL 260 L Indianapolis, IN 46202 Tel.: 1-317-274-4887, Fax: 1-317-274-9744.

Highlights► A synchrotron TXM tomography system was used to obtain morphology data of NMC electrodes. ► Geometric and electrochemical characteristics of the electrodes were analyzed. ► SEI and charge transfer resistances decrease with increasing NMC density. ► Increasing calendering causes crashing of NMC particles and decrease rate capability. ► Optimum performance is achieved at 3.0 g/cm^3 NMC density.

Abstract
The impact of calendering process on the geometric characteristics and electrochemical performance of LiNi$_{1/3}$Mn$_{1/3}$Co$_{1/3}$O$_2$ (NMC) electrode was investigated in this study. The geometric properties of NMC electrodes with different calendering conditions, such as porosity, pore size distribution, particle size distribution, specific surface area and tortuosity were calculated from the computed tomography data of the electrodes. A synchrotron transmission X-ray microscopy tomography system at the Advanced Photon Source of the Argonne National Laboratory was employed to obtain the tomography data. The geometric and electrochemical analysis show that calendering can increase the electrochemically active area, which improves rate capability. However, more calendering will result in crushing of NMC particles, which can reduce the electrode capacity at relatively high C rates. This study shows that the optimum electrochemical performance of NMC electrode at 94:3:3 weight ratio of NMC:binder:carbon black can be achieved by calendering to 3.0 g/cm^3 NMC density.

---

1. Introduction

During the last decade, Li ion batteries (LIBs) have become the main power source for electric vehicles and lots of research efforts have been done towards the development of new active electrode materials to improve the performance of LIBs. In addition to electrode material's electrochemical properties, the microstructure of composite electrodes determined by the fabrication process also plays a critical role in determining the performance of a LIB [1]. However, the impact of fabrication process on the performance of LIBs has not been widely explored [2]. In practice, many fabrication parameters are chosen based on experience rather than analysis and computation [2]. The fabrication of LIB electrode is a complex process involving many procedures, such as slurry preparation, coating, calendering, cell assembly, et al. All of the procedures could have significant impacts on the performance of a LIB. In this paper, we are going to focus on the impact of the calendering process.

Calendering is a process used in battery industry to adjust the porosity and thickness of electrode, smooth the surface roughness, and enhance conductivity. To this end, some research work has been done to study the impact of calendering process on electrochemical properties of LIB electrodes [3-12]. For instance, Zheng et al. investigated calendering effects on the physical and electrochemical properties of $LiNi_{1/3}Mn_{1/3}Co_{1/3}O_2$ (NMC) cathode [3, 7]. They found that the matrix conductivity is closely associated with the fraction of inactive material and weakly associated with the degree of calendering. Marks et al. have reported that compression on low carbon content NMC electrodes reduces the space between carbon chains and apparently increases conductivity [9].

However, there are few reports on the geometric characteristics and their impacts on the electrochemical performance of LIB electrodes with different calendering conditions due to the inhomogeneity, complexity, and three-dimensional (3D) nature of the electrode's microstructure. Recently, porous electrode microstructures have been reconstructed by advanced tomography techniques such as X-ray nano-computed tomography (nano-CT) [1, 13-22] and focused ion beam scanning electron microscope (FIB-SEM) tomography [11, 23, 24]. The reconstructed microstructures have been employed to investigate the geometric characteristics and electrochemical performance of LIB electrodes with different calendering conditions. For instance, Ebner et al. studied the influence of compression and carbon black and binder content on NMC cathode electrode porosity and discharge capacity using synchrotron radiation X-ray tomographic microscopy. Their results show that compression results in a porosity decrease by a factor of two, but has no significant impact on the high rate constant current discharge capacity [25]. The major advantage of their tomography system is the large field of view of the microscope, which can generate a very large

2

reconstruction volume to ensure the accuracy of structural analysis, especially for tortuosity. However, the voxel size of the synchrotron radiation X-ray tomographic microscopy used in Ebner's study is $370 \times 370 \times 370$ nm^3, which is not small enough to reveal the detailed microstructural information at smaller scales. In our recent publication, Lim et al. studied the geometric and electrochemical characteristics of lithium cobalt oxide (LiCoO$_2$) cathode electrode with different packing densities using a synchrotron transmission X-ray microscopy (TXM) tomography with voxel size of $58.2 \times 58.2 \times 58.2$ nm^3 [26]. They found that LiCoO$_2$ electrode with higher packing density shows larger capacity and better rate capability. Chen-Wiegart et al. studied the 3D morphology of a commercial LIB composite LiCoO$_2$-NMC positive electrode using a synchrotron TXM with voxel size of $38.9 \times 38.9 \times 38.9$ nm^3 [27, 28]. They found that the NMC particles have a much rougher surface compared to the LiCoO$_2$ particles. Cracks due to processing exist in both LiCoO$_2$ and NMC particles but the NMC particles exhibit more severe cracking and also tend to have internal pores in addition to radial cracks. In addition to experimental studies, the reconstructed microstructures have been utilized in electrochemical simulations to predict electrode performance. For instance, Mendoza et al. conducted coupled electrochemical-mechanical simulations based on 3D reconstruction of LiCoO$_2$ electrode and reported that the binder has a significant role in relaxing the overall stresses throughout the microstructure as well as at particle contacts [29].

NMC is one of the most successful LIB cathode materials and NMC LIBs have been widely accepted to be promising for electric vehicles. The commercial NMC particles usually have a spherical morphology with diameter around 10 μm and they are composed by sub-particles with size several hundred nanometers. Recently, several methods have been developed to tune the nanoscale structure of sub-particles to improve the performance of NMC electrode. For instance, Li et al. designed a facile nanoetching-template synthesis route to assign a porous nanomicrohierarchical morphology for NMC particles [30]. Peng et al. reported novel nanoarchitectured NMC cathodes composed of self-assembled nanosheet structures synthesized via a facile hydrothermal method and a stepwise calcination process [31]. Due to the unique microstructure of NMC particles and the knowledge obtained from the previous studies [25-28], we hypothesize that the impact of calendering on NMC electrode is different from LiCoO$_2$ shown in Ref [26]. Therefore, the purpose of this paper is to investigate the realistic geometric characteristics of NMC cathode electrode microstructures with different calendering conditions and their impacts on electrochemical performance using synchrotron TXM tomography with high spatial resolution. In this study, four NMC electrodes were fabricated from a same composition of materials, and calendered to an identical thickness under different loading of NMC. We reconstructed the porous microstructures of electrodes with different calendering conditions to examine geometric characteristics by employing synchrotron TXM tomography at the Advanced Photon Source (APS) of the Argonne National Laboratory (ANL). The electrodes were assembled in coin cells with a Li counter electrode for investigating the electrochemical characteristics. The impact of calendering condition

on the porous microstructure and electrochemical performance of NMC electrode is discussed based on the microstructural and electrochemical results.

2. Experimental

2.1 Materials

NMC active material was from Umicore, Brussels, Belgium; super-P carbon black (C65, TIMCAL Ltd.) was from MTI, Richmond, CA; polyvinylidene difluoride (KF 1120 polymer – 12 wt. % PVDF) binding agent was from Kureha, New York, NY; N-methyl-2-pyrrolidinone solvent (NMP, anhydrous 99.5%) was from Sigma-Aldrich, St. Louis, MO; EC/DEC Electrolyte containing 1M $LiPF_6$ in a 1:1 volume-ratio mixture of ethylene carbonate and dimethyl carbonate was received from BASF, Elyria, OH.

2.2 Electrode fabrication

To make electrode slurry, the active material, binder, and carbon black current conductor (94:3:3 of weight ratio) were added into NMP solution and mixed homogeneously by a magnetic stir bar in a vial for 20 h. Low percentage of binder and carbon black in the electrode is mainly due to the requirement of high capacity of LIB electrode and the invisibility of carbon and binder in synchrotron TXM [26]. The gel-like slurry was coated onto a thin aluminum foil via a film casting doctor blade (EQ-Se-KTQ-100, MTI, Richmond, CA, USA). The doctor blade was pre-set to a certain thickness to ensure each electrode on the current collector has a uniform thickness. By controlling the setting of the doctor blade, four different thicknesses of NMC electrode were coated on the current collector. The electrodes were then dried in an oven at 100°C for 0.5 h. Then they were pressed down to 50 μm using a rolling press machine (MR-100A, MTI, Richmond, CA, USA) (50 μm electrode is not pressed). A digital micrometer with 1 μm resolution (Digital micrometer-1IN/25MM, Marathon, Richmond Hill, ON, Canada) was used to measure the thickness of the electrodes before and after pressing. Finally, four 50 μm thick electrodes with various NMC densities were obtained. The electrodes were cut in 10 mm diameter and dried at 100°C in a vacuum oven for 10 h.

2.3 Cell assembly

The NMC electrodes were assembled using standard 2016 coin cell hardware with a 16 mm diameter Li metal sheet as the counter electrode, Celgard 2400 separator, and the liquid electrolyte in an argon-filled glovebox (under $O_2 < 0.1$ ppm, $H_2O < 0.1$ ppm; Unilab 2000, Mbraun, Stratham, NH, USA). The cell was sealed using a compact hydraulic crimping machine (MSK-110, MTI, Richmond, CA, USA) in the glove box. All the cells were aged for 10 h before the first charge to ensure full absorption of electrolyte into the pores of the electrode.

2.4 Electrochemical measurement

The coin cells were initially cycled three times between 3.0 and 4.2 V (vs. Li/Li+) under a constant current condition at 0.1 C rate. Then electrochemical impedance spectroscopy (EIS) tests were carried out at open circuit potential (4.2 V) using a two-electrode system with Li sheet as the counter electrode and NMC as the working electrode (CHI660D, CH instrument, Austin, TX, USA). Voltage amplitude was set to be 5 mV and frequency range was form 1,000,000 Hz to 0.01 Hz. ZView fitting

4

software was used to fit equivalent circuit parameters. After EIS testing, the cells were cycled for three times at different C rates to investigate electrode capacity and rate capability using a battery cycler (BT2000, Arbin, College Station, TX, USA). The influence of the impedance of Li counter electrode was described in our previous publication [26].

2.5 Synchrotron TXM tomography

The aluminum current collector was removed by soaking the electrode in 30% NaOH solution. After the electrode samples were cleaned by DI water and dried in air, they were cut to get a sharp edge using a sharp razor. Then a sample was mounted to the rotation stage of the synchrotron TXM at the beamline 32-ID-C at the APS of ANL for tomography scan. High energy level X-ray (8 keV) from the beamline was able to capture the projected X-ray images with 2 s exposure time at each 0.25° rotation increments over 180°. Flat field images with X-ray on and off were also taken for image processes. The total collection time for one electrode sample was 25 min.

2.6 Image processing

ImageJ was used to remove system errors of the projection images based on flat field images. Tomopy was used to transform the projection image dataset into 3D reconstruction data (image stack) with $58.2 \times 58.2 \times 58.2$ nm^3 voxel size. In addition, to analyze the electrode geometrically, image stack was processed to get binary data and reconstructed to 3D form by using Avizo software. Tetrahedral meshed microstructures of the electrodes were generated from the binary volumetric data with iso2mesh MATLAB algorithm [32]. The meshing algorithm extracted surface from a binary data and generated a surface mesh based on Delaunay refinement process. Tetrahedral volume mesh was generated from the surface mesh.

3. Results and discussion

3.1 Material volume fraction

By calendering process, four electrodes with different NMC densities, 1.9 g/cm^3, 2.6 g/cm^3, 3.0 g/cm^3 and 3.2 g/cm^3 were fabricated. The NMC density was calculated by electrode weight $\times$ NMC percentage / electrode volume. Electrode weight is measured by balance and NMC percentage is set to be 94% in our electrode. Electrode volume was calculated by electrode surface area $\times$ electrode thickness. The difference of the highest and lowest NMC density electrodes is shown in both X-ray CT images (Fig. 1a and b), 3D reconstructions (Fig. 1c and d) and SEM images (Fig. 1e, f, g and h). We can clearly see the carbon-binder matrix in SEM images. In the CT image, NMC particles are shown as white color. As shown in the CT images, NMC particles have very rough surface and most of the particles are not spherical. The particle morphology is similar to the ones shown in Chen-Wiegart's paper [28] but different from the ones shown in Ebner's paper [25]. The difference could be due to their large voxel size and different vendor of NMC material. To validate the reconstructed electrode microstructures, the volume fractions of the electrode components based on reconstructed microstructure are compared with the volume fractions based on the measured 10 mm diameter electrode's weight and thickness (Fig. 2). Since PVDF binder and carbon conductor have low X-ray attenuation, they cannot be distinguished from the pore phase.

Therefore, the volume fractions of PVDF binder and carbon conductor in Fig. 2 were calculated based on NMC material volume fraction, their weight fractions (94:3:3) and material densities ($\rho_{NMC} = 4.7 g/cm^3, \rho_c = 2g/cm^3, \rho_{binder} = 1.78 g/cm^3$). Volume fraction of a phase is calculated by the volume of the phase over the total volume. As shown in Fig. 2, the volume fractions from reconstructed CT data and weight measurement are consistent. We believe that the slight differences between them could be due to several reasons. First, the limited volume of the CT reconstruction and inhomogeneity of the electrode may cause an error. The reconstructed volumes are around $25 \times 25 \times 25$ μm^3, which is limited by the field of view of the TXM and sample preparation. Second, electrodes used for CT scan were cut, soaked and rinsed before the experiment, which may lose some particles and decrease the volume fraction of NMC. Third, the thickness of electrodes was measured by a digital micrometer with 1 μm resolution. Since the total thickness is 50 μm, theoretically there is a 2% measuring error.

3.2 Particle size distribution

As shown in Fig. 1b and d, with calendering percentage increasing, porosity is decreased, but many NMC particles are crushed to smaller sub-particles. To quantify this observed phenomenon, particle size distribution was calculated from equivalent spherical diameters of particles in the CT data labeled using Avizo 3D software. The frequency distributions of particle size (q_3) of the four different electrodes are shown in Fig. 3. The curve of 1.9 g/cm^3 electrode shows a normal distribution of particle size, which should be similar to the original NMC particles. The curves of the other three electrodes show larger distribution at larger size. We believe that it is mainly due to the resolution of TXM tomography (58.2 nm). Any gap smaller than this resolution cannot be detected. Since the particles are tightly packed at these two densities, some of them may be combined as a single large particle after CT reconstruction. However, the 3.2 g/cm^3 electrode has much higher distribution between 2 and 4 μm and lower distribution between 4 and 7 μm, which demonstrates that increasing calendering percentage crushed more NMC particles to sub-particles. The crushing of NMC particles could have a negative impact on the cell performance.

3.3 Pore size distribution

Pore size distribution (PSD) is an important parameter to characterize the morphology of porous LIB electrode [33]. In this study, PSD is quantified from the 3D binary CT data using the method described in Ref [20]. PSD of different NMC density electrodes and the corresponding box plot are shown in Fig. 4. The PSD results were calculated from the combined phase of pore and carbon-binder matrix because carbon and PVDF phases cannot be distinguished from the pore phase. The relative volume is defined as the total volume of a pore radius over the volume of the inactive phases including carbon, PVDF, and pore phases. The pore radii are positively skewed for all electrodes and tend to concentrate at smaller radius range with the increased NMC density. Fig. 4b shows box plots of pore radius of the different packing density electrodes. A box width is a range of pore radii from 25 to 75 percentiles and a centerline in the box indicates a

median radius at a corresponding NMC density. The median and box width are reduced with increasing NMC density. For instance, the relative pore volume of 1.9 g/cm^3 electrode has a wider inter quartile range (box width = 0.71 μm) with the median radius 1.12 μm and the maximum radius 3.16 μm. The relative pore volume of 3.2 g/cm^3 electrode has the narrowest box width 0.47 μm with the median radius 0.52 μm and the maximum radius 1.98 μm. It is noted that there should be pores smaller than 58.2 nm that cannot be detected by the synchrotron TXM. As we can predict from distribution data shown in Fig. 4a, the relative volume of those small pores should be very small. Although the carbon and PVDF phases cannot be distinguished from the pore phase, the result still can relatively demonstrate that the calendering process by the rolling press contributes more homogeneous distributions of pores and carbon-binder matrix.

3.4 Specific surface area

Specific surface area is the solid-electrolyte interface area of an electrode per bulk volume and it is important in LIB electrode because electrochemical reaction happens on the interface areas. In this study, the specific surface area can be obtained from the reconstructed microstructure. It should be noted that the specific surface area includes both the areas covered by carbon-binder matrix and open areas because the synchrotron TXM cannot distinguish carbon-binder phase from pore phase. Fig. 5a shows the specific surface area of the reconstructed electrodes and the homogeneous (spherical particle diameter is 5.2 μm) electrodes. The results show that the specific surface area increases with the volume fraction of NMC increasing. However, they don't show a clear linear relationship as the LiCoO$_2$ electrode [26]. We believe that it is mainly due to the different size distribution of NMC particles at different densities. For the 3.2 g/cm^3 electrode, the sub-particles generated by crushing increase the specific interface area. The CT images also show that the NMC particles have highly irregular shape and rough surface, which can increase the specific surface area. To investigate the effect of surface roughness of NMC particles on specific surface area, several large particles close to spherical shape were selected from the CT data. Fig. 5b and c show the 3D reconstruction of a NMC particle and a SEM image of a NMC particle, respectively. The images demonstrate that the synchrotron TXM tomography can capture the rough surface of NMC particles. The specific surface areas of the particles (surface area/particle volume) calculated from CT data are ~140% of the specific surface areas under spherical shape assumption. This important feature cannot be detected by other low resolution tomography techniques.

3.5 Tortuosity

Ion transport property in a porous electrode could be quantified by tortuosity (τ). Tortuosity has been considered as a function of porosity (ϵ) by Bruggeman relation $\tau = \epsilon^{-0.5}$. However, evidence has indicated that Bruggeman relation underestimates tortuosity in LIB electrode [26, 34]. In this study, tortuosity was calculated from the CT microstructure using the method proposed by Kehrwald et al. [34]. Fig. 6 shows that the tortuosity is very similar to the experimental results shown by Thorat [35] and much

higher than the tortuosity calculated by Bruggeman relation, at high NMC densities. At 1.9 g/cm^3 density, the tortuosity is close to the $LiCoO_2$ result [26], but it is still higher than Bruggeman relation. It should be noted that the tortuosity is underestimated by neglecting carbon and binder effects in this study. The larger tortuosity is mainly due to the highly irregular shape and the wide size distribution of NMC particles. It is severe at high NMC densities because of the crushing of NMC particles.

3.6 Electrochemical performance

The electrochemical performance of the electrodes with different NMC densities was investigated to study the geometric effects on LIB performance. For each density, multiple cells were fabricated and tested to ensure the repeatability of the electrochemical results. The cells with good capacity retention after rate capability testing were selected to demonstrate the electrochemical characteristics. Fig. 7 shows discharge profiles of the electrodes under various C rates cycled between 4.2 V and 3.0 V. Fig. 8 shows the discharge capacity of the different NMC density electrodes summarized as rate capability plot and Ragone plot. The capacity retention are all above 90% after the cycling experiment which indicates the discharging curves for different C rates in this experiment are reliable. As shown in Fig. 7, at low rate, such as 0.1 C, the four electrodes have similar discharge capacity. As the C rate increases, the capacity of all electrodes starts to decrease, which is normal. However, compared to 3.0 g/cm^3 and 2.6 g/cm^3 electrodes, 1.9 g/cm^3 and 3.2 g/cm^3 electrodes have much larger capacity drop. If we compare 1.9 g/cm^3 electrode and 3.2 g/cm^3 electrode, Fig. 7 shows that 1.9 g/cm^3 electrode has larger initial voltage drop due to its large interface resistance, while 3.2 g/cm^3 electrode has larger capacity loss. As a result, 1.9 g/cm^3 electrode has larger capacity than 3.2 g/cm^3 electrode at the C rates from 0.2 C to 1 C, but it has lower capacity than 3.2 g/cm^3 electrode due to the much larger ohmic loss at 2 C and 4 C. 3.2 g/cm^3 electrode still shows small capacity at these C rates, but 1.9 g/cm^3 electrode shows almost zero capacity. It is clear that the effect of NMC density on the capacity and rate capability of NMC electrode is different from $LiCoO_2$ electrode [26]. Ebner et al. showed similar discharge performance of NMC electrodes at different NMC densities [25]. However, the density range of their electrode is from 2.2 – 2.8 g/cm^3 electrode, which is narrower than the one in our experiment. In addition, the crushing of NMC particles is not obvious as shown in their images. Compared to our results, we think it is reasonable to have similar discharge performance in 2.2 – 2.8 g/cm^3 density range.

EIS results are used to further explain the effects of NMC density on rate capability. The impedance results of the EIS tests for different NMC density electrodes at 4.2 V are shown in Fig. 9. All four different density electrodes show two depressed semicircles when the frequencies progressed from high (left) to low (right). We believe that these EIS spectra represent same impedances as the $LiCoO_2$ electrode shown in our previous publication [26]. Briefly, the real axis (Z_0) intercept of the Nyquist plot at the high frequency is assigned as the ohmic resistance of the cell (R_e) by the electrolyte [3]. First semicircle in the high-to-mid frequency range is ascribed to the resistance (R_{sf}) by the SEI layer formed on the active material [36]. Second semicircle in the

8

mid-to-low-frequency range is ascribed to the charge transfer resistance (R_{ct}) at the electrolyte/electrode interface [37]. Warburg type impedance response (Z_w) at the low frequencies is considered as the solid-state diffusion of Li ions within the active material [37] and the electrolyte phase diffusion of Li ion [38]. In order to quantify the EIS spectra, equivalent circuit displayed in Table 1 was used to analyze the impedance spectra data. All the error percentage generated is lower than 10%, which verifies the validity of the equivalent circuit. As shown in Table 1, 1.9 g/cm^3 electrode has much larger R_{sf} and R_{ct} than the other three electrodes. 3.0 g/cm^3 and 3.2 g/cm^3 electrodes have the similar R_{sf} and R_{ct}. However, the rate capability of 3.2 g/cm^3 electrode is not the best. Since ohmic resistance (R_e) of the four electrodes is similar, we can conclude that the high tortuosity at high NMC density is not limiting the rate capacity of 3.2 g/cm^3 electrode. This phenomenon can be explained by the electrochemically active area theory proposed in our previous publication [26] and the crushing of NMC particles in 3.2 g/cm^3 electrode. The smaller pore size and uniform pore distribution cause more uniform distribution of conductive carbon-binder matrix and better contact between carbon-binder matrix and NMC particles, which lead to the increase of electrochemically active area. Thus, the R_{sf} and R_{ct} are reduced in the high NMC density electrodes and 3.0 g/cm^3 electrode has better rate capability than 1.9 g/cm^3 electrode. It should be noted that the conductivity of carbon-binder matrix can be degraded during cell cycling. Grillet et al. reported that ectrochemically-induced mechanical stresses degrade binder conductivity, increasing the internal resistance of the battery with cycling [39]. Although 3.2 g/cm^3 electrode also has low R_{sf} and R_{ct}, many NMC particles were crushed during calendering process. The nanometer-sized NMC particles were not connected well electronically and ionically, which can result in high impedance inside the particles. At low C rates, the capacity is not affected. However, at high C rates, many loosely connected nanometer-sized NMC particles become inactive and the capacity reduces significantly. This effect of calendering is different from $LiCoO_2$ electrode, which has the best performance at the highest $LiCoO_2$ density until the limitation of the calendering process is reached [26].

4. Conclusions

In this study, NMC cathode electrodes with different calendering conditions were investigated to obtain the correlation between the geometric characteristics and electrochemical performance. The 3D microstructure of NMC electrode was obtained by using the synchrotron TXM tomography with voxel size of $58.2 \times 58.2 \times 58.2$ nm^3 at beamline 32-ID-C at the APS of ANL. The geometric and electrochemical analysis show that more calendering can help to achieve smaller pore size and relatively uniform pore size distribution, thereby increasing the electrochemically active area. However, calendering also can cause crushing of NMC particles and deactivate the internal nanometer-sized particles at high C rates. At high calendering condition, the capacity drops significantly because many NMC particles are crushed. This study shows that the NMC electrode with the NMC density 3.0 g/cm^3 after calendering is the optimum when the weight ratio of NMC:binder:carbon is 94:3:3.

References

[1] C. Lim, B. Yan, L. Yin, L. Zhu,;1; Geometric Characteristics of Three Dimensional Reconstructed Anode Electrodes of Lithium Ion Batteries, Energies, 7 (2014) 2558-2572.

[2] J. Smekens, R. Gopalakrishnan, N. Van den Steen, N. Omar, O. Hegazy, A. Hubin, J. Van Mierlo,;1; Influence of Electrode Density on the Performance of Li-Ion Batteries: Experimental and Simulation Results, Energies, 9 (2016).

[3] H. Zheng, L. Tan, G. Liu, X. Song, V.S. Battaglia,;1; Calendering effects on the physical and electrochemical properties of Li [Ni 1/3 Mn 1/3 Co 1/3] O 2 cathode, J. Power Sources, 208 (2012) 52-57.

[4] A. van Bommel, R. Divigalpitiya,;1; Effect of calendering LiFePO4 electrodes, J. Electrochem. Soc., 159 (2012) A1791-A1795.

[5] G.-F. Yang, S.-K. Joo,;1; Calendering effect on the electrochemical performances of the thick Li-ion battery electrodes using a three dimensional Ni alloy foam current collector, Electrochim. Acta, 170 (2015) 263-268.

[6] G. Liu, H. Zheng, X. Song, V.S. Battaglia,;1; Particles and polymer binder interaction: a controlling factor in lithium-ion electrode performance, J. Electrochem. Soc., 159 (2012) A214-A221.

[7] H. Zheng, G. Liu, X. Song, P. Ridgway, S. Xun, V.S. Battaglia,;1; Cathode performance as a function of inactive material and void fractions, J. Electrochem. Soc., 157 (2010) A1060-A1066.

[8] W. Haselrieder, S. Ivanov, D.K. Christen, H. Bockholt, A. Kwade,;1; Impact of the Calendering Process on the Interfacial Structure and the Related Electrochemical Performance of Secondary Lithium-Ion Batteries, ECS Transactions, 50 (2013) 59-70.

[9] T. Marks, S. Trussler, A. Smith, D. Xiong, J. Dahn,;1; A guide to Li-ion coin-cell electrode making for academic researchers, J. Electrochem. Soc., 158 (2011) A51-A57.

[10] S. Ha, V.K. Ramani, W. Lu, J. Prakash,;1; Optimization of Inactive Material Content in Lithium Iron Phosphate Electrodes for High Power Applications, Electrochimica Acta, 191 (2016) 173-182.

[11] T. Hutzenlaub, S. Thiele, R. Zengerle, C. Ziegler,;1; Three-dimensional reconstruction of a LiCoO2 Li-ion battery cathode, Electrochemical and Solid-State Letters, 15 (2011) A33-A36.

[12] C. Lim, B. Yan, L. Yin, L. Zhu,;1; Geometric Characteristics of Three Dimensional Reconstructed Anode Electrodes of Lithium Ion Batteries, Energies, 7 (2014) 2558-2572.

[13] P. Shearing, L. Howard, P.S. Jørgensen, N. Brandon, S. Harris,;1; Characterization of the 3-dimensional microstructure of a graphite negative electrode from a Li-ion battery, Electrochem. Commun., 12 (2010) 374-377.

[14] R. Thiedmann, O. Stenzel, A. Spettl, P.R. Shearing, S.J. Harris, N.P. Brandon, V. Schmidt,;1; Stochastic simulation model for the 3D morphology of composite materials in Li–ion batteries, Computational Materials Science, 50 (2011) 3365-3376.

[15] C. Lim, B. Yan, L. Yin, L. Zhu,;1; Simulation of diffusion-induced stress using reconstructed electrodes particle structures generated by micro/nano-CT, Electrochim. Acta, 75 (2012) 279-287.

[16] Y.-c.K. Chen-Wiegart, P. Shearing, Q. Yuan, A. Tkachuk, J. Wang,;1; 3D morphological evolution of Li-ion battery negative electrode LiVO 2 during oxidation using X-ray nano-tomography, Electrochem. Commun., 21 (2012) 58-61.

[17] Y.-c.K. Chen-Wiegart, Z. Liu, K.T. Faber, S.A. Barnett, J. Wang,;1; 3D analysis of a LiCoO 2–Li (Ni 1/3 Mn 1/3 Co 1/3) O 2 Li-ion battery positive electrode using x-ray nano-tomography, Electrochem. Commun., 28 (2013) 127-130.

[18] S. Cooper, D. Eastwood, J. Gelb, G. Damblanc, D. Brett, R. Bradley, P. Withers, P. Lee, A. Marquis, N. Brandon,;1; Image based modelling of microstructural heterogeneity in LiFePO 4 electrodes for Li-ion batteries, J. Power Sources, 247 (2014) 1033-1039.

[19] S.K. Babu, A.I. Mohamed, J.F. Whitacre, S. Litster,;1; Multiple imaging mode X-ray computed tomography for distinguishing active and inactive phases in lithium-ion battery cathodes, J. Power Sources, 283 (2015) 314-319.

[20] B. Yan, C. Lim, L. Yin, L. Zhu,;1; Three dimensional simulation of galvanostatic discharge of LiCoO2 cathode based on X-ray nano-CT images, Journal of The Electrochemical Society, 159 (2012) A1604-A1614.

[21] B. Yan, C.W. Lim, Z.B. Song, L.K. Zhu,;1; Analysis of Polarization in Realistic Li Ion Battery Electrode Microstructure Using Numerical Simulation, Electrochimica Acta, 185 (2015) 125-141.

[22] B. Yan, C. Lim, L. Yin, L. Zhu,;1; Simulation of heat generation in a reconstructed LiCoO$_2$ cathode during galvanostatic discharge, Electrochimica Acta, 100 (2013) 171-179.

[23] J.R. Wilson, J.S. Cronin, S.A. Barnett, S.J. Harris,;1; Measurement of three-dimensional microstructure in a LiCoO 2 positive electrode, J. Power Sources, 196 (2011) 3443-3447.

[24] Z. Liu, J.S. Cronin, K. Yu-chen, J.R. Wilson, K.J. Yakal-Kremski, J. Wang, K.T. Faber, S.A. Barnett,;1; Three-dimensional morphological measurements of LiCoO 2 and LiCoO 2/Li (Ni 1/3 Mn 1/3 Co 1/3) O 2 lithium-ion battery cathodes, J. Power Sources, 227 (2013) 267-274.

[25] M. Ebner, F. Geldmacher, F. Marone, M. Stampanoni, V. Wood,;1; X-ray tomography of porous, transition metal oxide based lithium ion battery electrodes, Advanced Energy Materials, 3 (2013) 845-850.

[26] C. Lim, B. Yan, H. Kang, Z. Song, W.C. Lee, V. De Andrade, F. De Carlo, L. Yin, Y. Kim, L. Zhu,;1; Analysis of geometric and electrochemical characteristics of lithium cobalt oxide electrode with different packing densities, Journal of Power Sources, 328 (2016) 46-55.

[27] Z. Liu, J.S. Cronin, Y.C.K. Chen-Wiegart, J.R. Wilson, K.J. Yakal-Kremski, J. Wang, K.T. Faber, S.A. Barnett,;1; Three-dimensional morphological measurements of

LiCoO2 and LiCoO2/Li (Ni1/3Mn1/3Co1/3)O-2 lithium-ion battery cathodes, Journal of Power Sources, 227 (2013) 267-274.

[28] Y.C.K. Chen-Wiegart, Z. Liu, K.T. Faber, S.A. Barnett, J. Wang,;1; 3D analysis of a LiCoO2-Li(Ni1/3Mn1/3Co1/3)O-2 Li-ion battery positive electrode using x-ray nano-tomography, Electrochemistry Communications, 28 (2013) 127-130.

[29] H. Mendoza, S.A. Roberts, V.E. Brunini, A.M. Grillet, Mechanical and;1; Electrochemical Response of a LiCoO2 Cathode using Reconstructed Microstructures, Electrochimica Acta, 190 (2016) 1-15.

[30] L. Li, L.C. Wang, X.X. Zhang, M. Xie, F. Wu, R.J. Chen, Structural and;1; Electrochemical Study of Hierarchical LiNi1/3Co1/3Mn1/3O2 Cathode Material for Lithium-Ion Batteries, Acs Applied Materials & Interfaces, 7 (2015) 21939-21947.

[31] L.L. Peng, Y. Zhu, U. Khakoo, D.H. Chen, G.H. Yu,;1; Self-assembled LiNi1/3Co1/3Mn1/3O2 nanosheet cathodes with tunable rate capability, Nano Energy, 17 (2015) 36-42.

[32] Q.Q. Fang, D.A. Boas, Ieee,;1; TETRAHEDRAL MESH GENERATION FROM VOLUMETRIC BINARY AND GRAY-SCALE IMAGES, 2009.

[33] M. Endo, T. Maeda, T. Takeda, Y. Kim, K. Koshiba, H. Hara, M. Dresselhaus,;1; Capacitance and pore-size distribution in aqueous and nonaqueous electrolytes using various activated carbon electrodes, Journal of the Electrochemical Society, 148 (2001) A910-A914.

[34] D. Kehrwald, P.R. Shearing, N.P. Brandon, P.K. Sinha, S.J. Harris,;1; Local tortuosity inhomogeneities in a lithium battery composite electrode, J. Electrochem. Soc., 158 (2011) A1393-A1399.

[35] I.V. Thorat, D.E. Stephenson, N.A. Zacharias, K. Zaghib, J.N. Harb, D.R. Wheeler,;1; Quantifying tortuosity in porous Li-ion battery materials, Journal of Power Sources, 188 (2009) 592-600.

[36] M. Levi, G. Salitra, B. Markovsky, H. Teller, D. Aurbach, U. Heider, L. Heider,;1; Solid-State Electrochemical Kinetics of Li-Ion Intercalation into Li1− x CoO2: Simultaneous Application of Electroanalytical Techniques SSCV, PITT, and EIS, J. Electrochem. Soc., 146 (1999) 1279-1289.

[37] M. Thomas, P. Bruce, J. Goodenough,;1; AC Impedance Analysis of Polycrystalline Insertion Electrodes: Application to Li1− x CoO2, J. Electrochem. Soc., 132 (1985) 1521-1528.

[38] J. Huang, Z. Li, J.B. Zhang, S.L. Song, Z.L. Lou, N.N. Wu,;1; An Analytical Three-Scale Impedance Model for Porous Electrode with Agglomerates in Lithium-Ion Batteries, Journal of the Electrochemical Society, 162 (2015) A585-A595.

[39] A.M. Grillet, T. Humplik, E.K. Stirrup, S.A. Roberts, D.A. Barringer, C.M. Snyder, M.R. Janvrin, C.A. Apblett,;1; Conductivity Degradation of Polyvinylidene Fluoride Composite Binder during Cycling: Measurements and Simulations for Lithium-Ion Batteries, Journal of the Electrochemical Society, 163 (2016) A1859-A1871.

Fig. 1. 2D CT images of (a) 1.9 g/cm^3 electrode and (b) 3.2 g/cm^3 electrode obtained by the synchrotron TXM tomography. The bright color region represents NMC particles. 3D CT reconstruction with a volume of $23 \times 23 \times 23$ μm^3 of (c) 1.9 g/cm^3 electrode and (d) 3.2 g/cm^3 electrode obtained by Avizo. SEM images of (e) 1.9 g/cm^3 electrode, (f) 3.2 g/cm^3 electrode, (g) cross-section of 1.9 g/cm^3 electrode, and (h) cross-section of 3.2 g/cm^3 electrode.

Fig. 2. Volume fractions of NMC and pore+C+PVDF calculated from the reconstructed porous microstructures (left) and the loadings of the different NMC density electrodes (right).

Fig. 3. Particle size distribution obtained from the labeled tomography data of the porous electrodes with four different NMC densities.

Fig. 4. a) Pore size distribution of the different NMC density electrodes calculated from the reconstructed microstructure with the voxel size of $58.2 \times 58.2 \times 58.2$ nm^3 and b) the corresponding box plot.

Fig. 5. (a)Specific surface area of the reconstructed electrodes and the homogeneous (spherical particle diameter is 5.2 μm) electrodes with the different volume fraction of the active material. (b) 3D reconstruction of a NMC particle in the electrode with rough surface. (c) SEM image of a NMC particle showing rough surface.
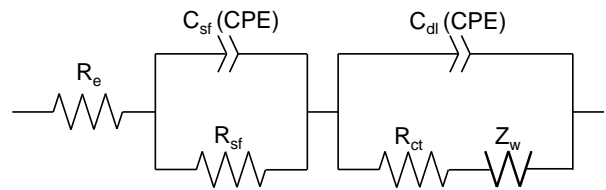
Fig. 6. Tortuosity of the reconstructed electrodes compared with the Bruggeman relation and previously reported results ($\tau = 1.8\varepsilon^{-0.53}$ [35]) and ($\tau = \varepsilon^{-1.074}$ [26]).

Fig. 7. Discharge profiles of the different NMC density electrodes measured at (a) 0.1 C rate, (b) 1 C rate and (c) 4 C rate.

Fig. 8. Discharge performance of the different NMC density electrodes summarized as a) Rate capabilities plot and b) Ragone plot.

Fig. 9. AC impedance results plotted for the different NMC density electrodes at 4.2 V.

Table caption Table 1. Internal resistances of the different NMC density electrodes at 4.2 V and the equivalent circuit.

Packing Density [g/cm^3]	R_e [Ω]	R_e error [%]	R_{sf} [Ω]	R_{sf} error [%]	R_{sf} normalized [Ω*g/cm^3]	R_{ct} [Ω]	R_{ct} error [%]	R_{ct} normalized [Ω*g/cm^3]
1.9	5.1	1.3	83.4	7.8	158.48	101.2	7.4	192.28
2.6	10.9	0.56	31.8	4.2	82.39	13.24	5.56	34.42
3.0	9.2	0.8	7.1	3.8	21.3	6.8	5.8	20.28
3.2	6.6	1.7	3.2	7.0	10.24	7.2	3.9	22.91

TDENDOFDOCTD